Advances in Science and Technology Research Journal

Advances in Science and Technology Research Journal, 2025, 19(1), 48–71
https://doi.org/10.12913/22998624/193764
ISSN 2299-8624, License CC-BY 4.0

Received: 2024.06.10
Accepted: 2024.11.15
Published: 2024.12.01

Improving the mechanical properties of structural elements made of titanium, aluminum alloys, and steel through the additive manufacturing application

Karolina Karolewska[1], Grzegorz Szala[2], Małgorzata Trepczyńska-Łent[1], Bogdan Ligaj[3]

[1] Faculty of Mechanical Engineering, PBS Bydgoszcz University of Science and Technology, al. Prof. S. Kaliskiego 7, 85-796 Bydgoszcz, Poland
[2] Kazimierz Wielki University, Faculty of Mechatronics, ul. Kopernika 1, 85-074 Bydgoszcz, Poland
[3] BSW University of Bydgoszcz, ul. Unii Lubelskiej 4C 85-059 Bydgoszcz, Poland
* Corresponding author's e-mail: karolina.karolewska@pbs.edu.pl

ABSTRACT

The research paper discussed the analysis of mechanical properties such as tensile strength, yield strength, Young's modulus, and elongation, as well as microstructural and hardness tests of three materials commonly used in additive manufacturing. The selected materials were 316L steel, AlSi10Mg aluminum alloy, and Ti6Al4V titanium alloy. The mechanical properties were evaluated using strain gauge measurements and digital image correlation, allowing for the determination of local material properties. The conducted research revealed that sample fractures were caused by the defects resulting from the manufacturing process, often along the boundaries of sequentially deposited layers. However, tensile tests demonstrated that the tensile strength of additive manufactured components is comparable to or higher than those produced using traditional manufacturing techniques. The research results indicated the potential for utilizing additive manufacturing technology in the production of structural components under static loading conditions.

Keywords: DMLS, additive manufacturing, HV10 hardness, material strength, static loads, Ti6Al4V, AlSi10Mg, 316L, DIC.

INTRODUCTION

The most important feature of additive manufacturing (AM) is the ability to produce complex metal parts without the need for additional machining processes. This significantly reduces the production time of finished parts. For this reason, AM is becoming more and more competitive with classic manufacturing techniques, i.e. forging and casting. Most standard manufacturing techniques involve material removal processes, which remove excess material to produce the component. This means that the amount of material used in the process is much greater than that from which the element itself is made. AM technologies gain an advantage due to the fact that they are able to produce much less waste and therefore use less material [1–4]. Currently, SLS and SLM are some of the most popular AM processes for making metal parts. The first one involves selective laser sintering, while the second one requires full melting of subsequent layers. Differences in technologies may result in slightly different microstructures resulting from different process settings and, therefore, mechanical properties. Laser power, spot size and scanning speed are very important in the manufacturing process [5, 6]. The optimal combination of process parameters allows for obtaining the appropriate laser power density, which results in the production of a high-strength element [7]. High laser power density can increase the density of the manufactured element and minimize the porosity defects created during the process. The material can vaporize at too high laser powers, through the high cooling rates typical of additive manufacturing, while existing and accumulating as a gas in the molten material layer, creating a porous structure. Too low laser energy density contributes to defects in the form of points of unmelted material, creating discontinuities and porosity [8–11]. According to [12, 13], the optimal laser energy density is 120 J/mm^3, which allows for minimizing internal defects and achieving full density. Moreover, the laser beam diameter and the layer scanning method, which are related to the laser path during the manufacturing process, also influence the durability. The layers should be applied by changing the scanning angle between them, due to the reduction of material anisotropy caused by temperature gradients [14–19]. Changing the scanning direction corresponds to a different direction of the temperature gradient, which is related to the directionality of the microstructure and can significantly affect the mechanical properties of the manufactured element [14, 20].

Temperature gradients also cause residual stresses in the manufactured elements. They appear by reducing heat conduction through the powder due to the rapid heating of the last applied layer relative to the layers located below it. The second mechanism of residual stress formation is the phase transformation resulting from solidification processes. These stresses contribute to lower resistance to deformation, reduced static and dynamic strength, as well as low fatigue strength [14, 20–22].

The surface geometric structure is also one of the factors that influence the strength of parts manufactured using additive methods. A high value of the roughness parameter may cause the formation of cracks and their propagation. The surface geometric structure of elements obtained using AM depends mainly on the thickness of the applied layer, the powder grains size, and the printing process parameters. The geometric structure of the surface can also be changed by reducing the diameter of the powder used, as well as increasing the laser energy density. The value of the surface roughness parameter may be influenced by unmelted powder that adheres to the sintered element [23, 24].

The authors [15, 25–36] point to a strong dependence of the strength of elements made using additive technology on the angle of their position relative to the printing direction. The lowest values of mechanical and fatigue properties are found in elements made at an angle of 90°, while the highest values are those produced at an angle of 45°. Build direction affects the way the fused or sintered layers are arranged. This translates into the obtained microstructure and grain growth direction, which is related to strength parameters. The strength of structural elements made of AM is therefore influenced by many factors, such as the quality of the powdered material, build direction, geometric structure of the surface, etc.

Currently, additive technologies allow the production of structural elements from many types of materials, including: aluminum alloys (e.g. AlSi10Mg, AlF257), stainless steels (e.g. 316L, 17-4PH, PH1, CX), tool steels (e.g. MS1, CX), copper alloys (e.g. CuCrZr) or nickel alloys (e.g. IN625, IN718). Some of the most popular materials used in additive manufacturing are Ti6Al4V titanium alloy, 316L stainless steel and AlSi10Mg aluminum alloy.

Table 1 summarizes the mechanical properties of selected materials produced using various additive manufacturing methods– direct metal laser sintering (DMLS), selective laser melting (SLM), electron beam melting (EBM), and laser metal deposition (LMD).

Among the methods used for manufacturing metal components, LMD is the least popular. Its main applications include repairing damaged structural elements and producing large-sized parts. However, the main drawback of the method is the surface quality and the need for additional post-processing. Powder Bed Fusion methods (DMLS, SLM, EBM) are highly popular due to their capability to produce fully dense elements. DMLS and SLM methods are known for their superior mechanical properties, high accuracy in manufacturing, and good surface quality. The EBM method allows for a quicker production of an element compared to DMLS or SLM, however, it does result in lower accuracy. The EBM technology only enables the manufacturing of parts from a limited range of materials, which is SLM and DMLS are more commonly used [87].

Table 1 presents characterization of the influence of sample printing parameters using the additive method for materials such as titanium alloy Ti6Al4V, aluminum alloy AlSi10Mg and 316L steel. It reveals that the mechanical properties of alloys are significantly influenced by the heat treatment and the adopted parameters of the manufacturing process.

An important assumption of the use of additive technology is to obtain a material with strength no lower than that of the material produced by the conventional method. The adoption of such an assumption is safe due to the design of structural

Table 1. Mechanical properties of materials 316L, AlSi10Mg and Ti6Al4V produced using additive methods

Material	Autor	Technology	Build direction	Heat treatment	σ_u	$\sigma_{y0.2}$	A	E	Hardness
					MPa	MPa	%	GPa	-
316L	[28]	DMLS	0	Stress relief	717	489	28	180	-
			45	Stress relief	680	473	30	193	-
	[25]	SLM	90	As-built	565	462	53.7	-	-
				Annealing	595	443	48.6	-	-
	[37]	SLM	0	-	604	318	39.8	161.6	-
			45	-	659	376	44.0	152.7	-
			90	-	517	226	29.4	148.4	-
	[38]	SLM	-	-	592	235	53.1	196.2	-
	[39]	SLM	90	-	697-713	530-551	32.4-43.6	-	-
			105	-	714-717	566-570	40.6-42.8	-	-
			120	-	682-685	540-545	36.5-37.9	-	-
			135	-	697-693	541-556	36.6-38.4	-	-
			150	-	698-709	534-555	39.6-40.4	-	-
	[40]	SLM	-	As-built	1016	550	50	-	-
	[41]	SLM	-	-	551	-	49.5	45.0	232 HV0.3
	[42]	SLM	90	-	567	-	23.8	-	235 HV
		SLM	-	As-built	752	638	41.2	-	-
			-	Annealing	673	424	43.9	-	-
			-	Annealing	684	416	51.6	-	-
	[75]	EBM	90	As-built	800	577	36.0	-	178 HV
	[76]	EBM	-	-	509	253	59.0	-	-
	[77]	LMD	90	As-built	647	518	20.0	-	-
	[78]	LMD	90	As-built	600	387	-	-	37 HRC
			90	Annealing	567	310	-	-	40 HRC
			0	As-built	665	473	-	-	38 HRC
			0	Annealing	633	378	-	-	35 HRC
AlSi10Mg	[28]	DMLS	0	Stress relief	358	227	3.9	65.5	-
			90		289	172	2.6	75.4	-
	[43]	SLM	0	HIP	315	225	1.3	-	-
			90		345	250	1.0	-	-
	[44]	SLM	-	-	245-331	-	-	-	-
	[45]	SLM	0	-	460	264	6.4	83.5	-
			45	-	463	268	7.4	82	-
			90	-	473	244	6.8	81	-
	[46]	DMLS	35,5	-	278	155	2.64	46.4	-
			45	-	331	169	2.82	51.1	-
			60	-	336	172	2.89	53.0	-
			90	-	361	176	2.92	54.2	-
	[47]	DMLS	0	As-built	481	314	3.3	-	137 HV
			0	Stress relief	395	276	5.0	-	103 HV
	[79]	LMD	-	-	209	107	6.8	-	-

Cont. Table 1

Ti6Al4V	[28]	DMLS	0	Stress relief	1130	1096	1.2	114.9	-
			90	Stress relief	1034	972	5.5	108.8	-
			90	HIP	931	862	24.0	111.7	-
	[8]	DMLS	-	-	1195	952	7.4	-	-
	[48]	DMLS	90	As-built	1262	1084	6.1	-	37 HRC
			90	Annealing	1126	1070	5.1	-	40 HRC
	[27]	DMLS	0	As-built	1370	1275	6.5	-	365 HV0.1
			90	As-built	1269	1201	4.9	-	463 HV0.1
	[49]	DMLS	90	As-built	1241	1065	6.0	120.1	385 HV0.2
			90	Annealing	1223	996	7.0	117.5	367 HV0.2
			90	HIP	941	839	19.0	115.3	339 HV0.2
	[50]	SLM	-	As-built	1092	102	16.5	112.7	-
			-	HIP	962	850	22.5	108.7	-
	[51]	SLM	-	As-built	1051	986	10.9	112.4	360 HV0.1
			-	Annealing	988	908	9.5	118.8	324 HV0.1
			-	HIP	973	885	19.0	115.4	321 HV0.1
	[80]	EBM	-	As-built	1002	902	6.5	113.3	380 HV
			-	HIP	796	785	5.9	109.4	530 HV
	[81]		0	As-built	825	730	7.7	100	330 HV
			90	As-built	725	650	8.6	95	330 HV
	[82]		90	As-built	955	869	9.8	-	-
			0	As-buil	987	891	15.7	-	-
	[83]		0	As-built	915	853	-	98.8	-
			45	As-built	918	859	-	107.9	-
			90	As-built	919	857	-	104.8	-
	[84]	LMD	90	As-buil	1094	984	4.2	-	-
			0	As-built	1151	1041	2.2	-	-
	[85]		90	As-built	1025	950	5.0	-	-
			0	As-built	1025	950	12.0	-	-
			-	Annealing	920	850	17.0	-	-
	[86]		90	As-built	1032	916	19.0	-	-
			0	As-built	1072	961	17.0	-	-

elements by designers, who can base on the general properties of specific types of materials.

The aim of the work was to present the results and comparative analysis of the mechanical properties of selected metal alloys, i.e. Ti6Al4V, AlSi10Mg and 316L produced using the additive method. The tests were carried out under static load conditions.

RESEARCH MATERIAL AND METHODOLOGY

The research focused on three types of materials that are highly popular and extensively utilized for manufacturing structural components using AM. The mechanical properties tests of specimens manufactured using the additive method were performed on two non-ferrous metal alloys: Ti6Al4V and AlSi10Mg and 316L. Ti6Al4V is one of the most used materials in metal 3D printing. The tests were carried out on a two-phase α + β titanium alloy, the chemical composition of which is presented in Table 2 in accordance with the ASTM F2924-14 standard [52]. The main alloying element of this material is an aluminum. It stabilizes the α and β phases, usually assuming intermediate properties. These alloys are characterized by better mechanical properties compared to α alloys; however, they have worse properties at higher temperatures [53]. The Ti6Al4V research material was chosen due to

Table 2. Chemical composition of Ti6Al4V [52]

Main alloying elements and their content in the Ti6Al4V, in wt. %								
Al	V	Fe	O	C	N	Y	Other	Ti
5.5÷6.8	3.5÷4.5	≤ 0.3	≤ 0.2	≤ 0.08	≤ 0.05	≤ 0.005	≤ 0.4	Rest

its wide range of applications in many industries [8, 50, 54–58].

A commonly used material for the production of structural elements using additive technologies is the AlSi10Mg (EN AW-4046). This material combines adequate strength with thermal properties and low density (ρ ≈ 2.75 kg/dm^3). Moreover, it is characterized by excellent casting properties. These properties allow the use of structural elements subject to high loads. AlSi10Mg is used to create thin-walled castings with complex geometry and, due to its properties, is often used in the automotive, aviation and automation industries. Printed elements can be subject to various types of processing, such as welding, painting or polishing [59–63].

Table 3 presents the chemical composition of the aluminum alloy in relation to the ASTM F3318-18 standard [64].

Stainless steel 316L (X2CrNiMo17-12-2, 1.4404, AISI 316L) is also used in additive processes. It is characterized by high deformity and desirable thermal properties. This material can be used for machine components in contact with food, medical devices, etc. 316L is a low-carbon alloy that is defined by good mechanical properties, machinability, wear resistance, and excellent anti-oxidation and anti-corrosion features. Hardening, tempering, annealing and normalization are types of heat treatment that are regularly used to obtain specific microstructures and desired mechanical properties of this type of steel. The mechanical properties of material depend on its microstructure, which is influenced by phase transformations, precipitation and recrystallization. However, in these metal alloys, hardness and strength can be enhanced by generating a high density of dislocation within the grains [40, 65–67].

The chemical composition of 316L is provided in Table 4 according to the ASTM F3184 standard [68].

The experiments under static load conditions were carried out on specimens prepared in

Table 3. Chemical composition of AlSi10Mg [64]

Main alloying elements and their content in the AlSi10Mg, in wt. %										
Si	Fe	Cu	Mn	Mg	Ni	Zn	Pb	Sn	Ti	Al
9÷11	0÷0.055	0÷0.1	0÷0.45	0.20÷0.45	0÷0.05	0÷0.10	0÷0.05	0÷0.05	0÷0.15	rest

Table 4. Chemical composition of the 316L stainless steel [68]

Main alloying elements and their content in the 316L, in wt. %										
Cr	Ni	Mo	Mg	Si	N	O	P	C	S	Fe
16÷18	10÷14	2.0÷3.0	≤ 2.0	≤ 1.0	≤ 0.1	≤ 0.1	≤ 0.045	≤ 0.03	≤ 0.03	rest

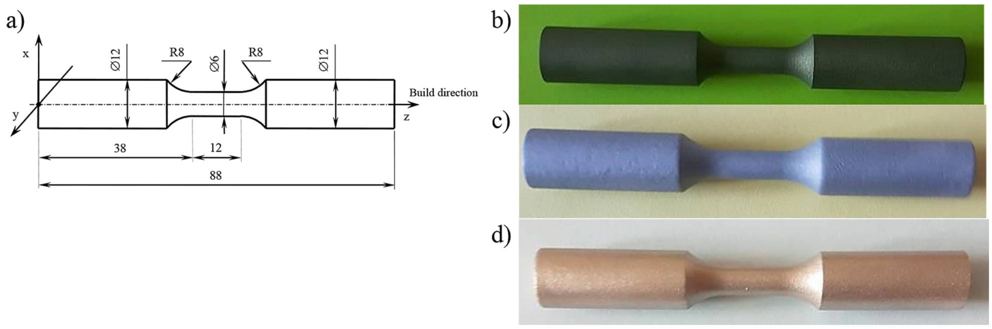

Figure 1. Sample for strength tests under static loads condition: a) with geometric dimensions; physical form of the sample made from: b) Ti6Al4V, c) AlSi10Mg, d) 316L

accordance with the recommendation of the Polish standard PN-74/H-04327 [90]. The geometric shape of samples along with their dimensions is shown in Figure 1a. The test objects were made using AM technology from three types of material: Ti6Al4V (Figure 1b), AlSi10Mg (Figure 1c), and 316L (Figure 1d).

The specimens for tests under static load conditions were created using AM technology known as laser sintering. This method was chosen for its ability to achieve high mechanical properties, excellent surface quality, accuracy, and complete density of the produced components. The build direction of all samples was vertical, and in the further part of the article it will be referred to as aligned with the z-axis. The samples made of Ti6Al4V were printed on an EOS M280 device with a working platform size of 250 × 250 × 325 mm. The printing process was characterized by the following parameters: laser power of 200 W, minimum layer thickness of 20 ÷ 75 µm, scanning speed of up to 7 m/s. The element build direction was aligned with the z-axis.

In Figure 2, the laser's working path for creating each layer of the samples is depicted in schematic manner. The specimens were made of AlSi10Mg using a device with a working platform size of 500 × 280 × 365 mm. The laser maximum power was 400 W. The layer thickness ranged from 20 to 75 µm. The spot size during printing was 100 µm. The maximum scanning speed was 10 m/s. The build direction of the component was in line with the z-axis.

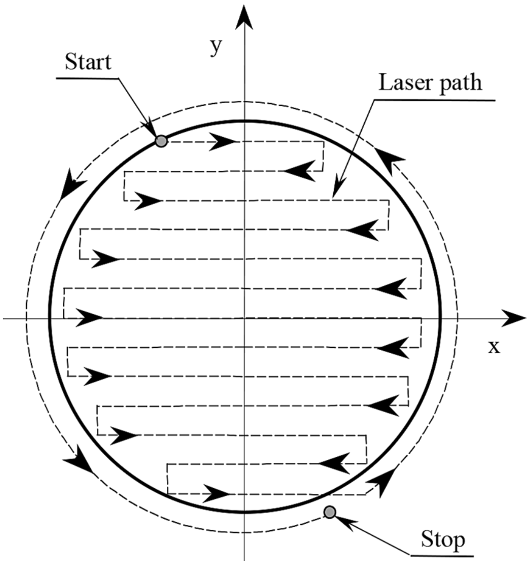

Figure 2. Schematic of laser beam movement during the sintering process of a single specimen layer [58]

The steel samples were produced on a ProX DMP 320 printer, which had a working platform size of 275 × 275 × 420 mm. The element symmetry axis was aligned with z-axis. The thickness of the applied layer was 20 to 75 µm, and the spot size was 60 µm. The laser power during printing was variable and was adjusted for each layer, reaching a maximum value of 500 W.

The strength tests were performed at the Materials and Structures Research Laboratory, which is affiliated with the Faculty of Mechanical Engineering at the Bydgoszcz University of Science and Technology.

The static tensile test was carried out following the guidelines of the PN-EN ISO 6892-1:2016 standard [91]. The controlling parameter during the experimental research was the displacement of the machine's piston, which was set at a rate of 0.05 mm/s. The tests included measuring the applied load force and deformation. The material testing was performed on an Instron 8502 strength testing machine, where experiments were done using a 10 mm gauge length extensometer and a measurement range of 1 mm.

Throughout the static tensile test of different materials: Ti6Al4V, AlSi10Mg, and 316L, deformations were measured using two methods. The first one involved the use of a traditional extensometer, which was directly installed on the test specimen, and a more precise technique known as digital image correlation. By using the non-contact optical DIC method, it is possible to measure displacements in a plane, which can be used to determine deformations of a structural elements caused by external loads [69–73].

The static tests using DIC consistent of measuring and monitoring displacements of the observed section of the specimen, which was in the camera's field of view. The BASLER acA4024-8gm camera was positioned on a tripod placed on a stable surface. The measurement using DIC consisted of periodically recording a series of images at a defined time, with the first image serving as the reference image. The method used involved taking photos of the sample during the tensile test using a camera at regular time intervals. The recorded images were then analyzed for displacement using BASLER's Pylon software. This program compared all the images captured during the test to a reference image. This process involved identifying the position of a specific pixel on the reference image and tracking its movement on the successive photos.

The hardness of samples produced by AM from Ti6Al4V, AlSi10Mg, and 316L was measured using the Vickers method. This measurement was conducted in accordance with ISO 6507-1:2018 [92].

The research setup for hardness testing was equipped with HUATEC hardness tester. The applied load during the tests was 98.07 N, which corresponded to a hardness value on the HV10 scale.

The samples for metallographic studies were taken from specimens subjected to static loads. The collected samples were covered in epoxy resin and then polished. The prepared samples for microstructural analysis were treated with etching processes. The Ti6Al4V samples were treated with Kroll's reagent, which had the following chemical composition: 68 cm^3 H_2O + 16 cm^3 HNO_3 + 16 cm^3 HF. Keller's reagent, with the following composition, was used to etch: 25 cm^3 HNO^3 + 15 cm^3 HCl + 5 cm^3 HF + 955 cm^3 H_20. Meanwhile, 316L stainless steel was treated with a reagent having a specified composition: 6 cm^3 HCl + 4 cm^3 HNO_3 + 4 cm^3 CH_3COOH + 0.2 cm^3 $C_3H_8O_3$.

Microstructure images were taken from longitudinal and transverse sections of samples using a Nikon ECLIPSE MA100 optical microscope.

RESEARCH RESULTS

Material strength under static loads

On the basis of the research conducted under static load conditions, the mechanical properties of the materials (Ti6Al4V, AlSi10Mg, 316L) were determined: tensile strength σ_u, yield point $\sigma_{y0.2}$, Young's modulus E, elongation A and reduction of area Z. During the static tensile test, the strain value ε was measured by the use of two different approach. The first method involved using a strain gauge directly attached to the specimen. The second one measured strain in the specimen using DIC method. Figure 3 indicates the areas in the measurement section of the sample that were subject to displacement analysis. The extensometer had a measurement range of L4 = 10 mm, while the measurement ranges for the DIC digital image correlation method were: L1 = 1.36 mm, L2 = 2.72 mm, L3 = 3.49 mm [74]. The results obtained for Ti6Al4V, AlSi10Mg, 316L, through measurements using extensometer and DIC method, were compared with the mechanical properties of these materials specified in the ISO 6892-1:2016 standard [91]. The normative strength parameters used in the material research are presented in Table 5.

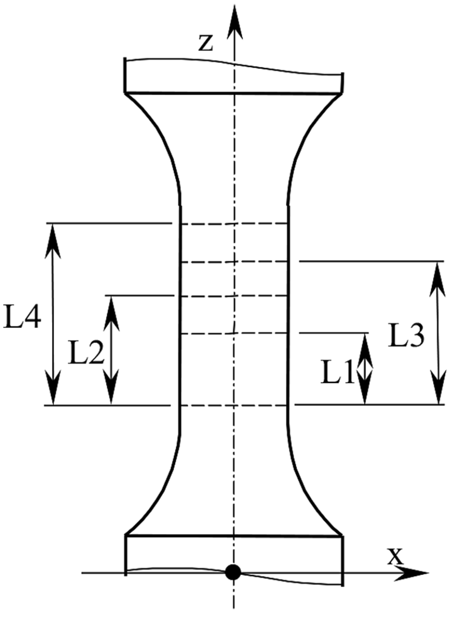

Figure 3. Schematic representation of the areas analyzed using the digital image correlation (DIC) method: L1 = 1.36 mm, L2 = 2.72 mm, L3 = 3.49 mm, L4 = 10 mm [74]

In Figure 4 there are sample tension graphs obtained by the use of an extensometer and DIC method. The test results obtained using the classical extensometer differ from the results for the DIC method. In the case of the Ti6Al4V, strength-related parameters such as: yield point

Table 5. Mechanical characteristics of selected metal alloys based on manufacturer's catalogs

Material	Mechanical properties			
	σ_u	$\sigma_{y0.2}$	E	A
	MPa	MPa	GPa	%
1	2	3	4	5
Ti6Al4V	1160±30	1050±50	105±5	5.5±2
AlSi10Mg	460±20	260±20	75±10	6±2
316L	507±26	464±26	167±26	40±5

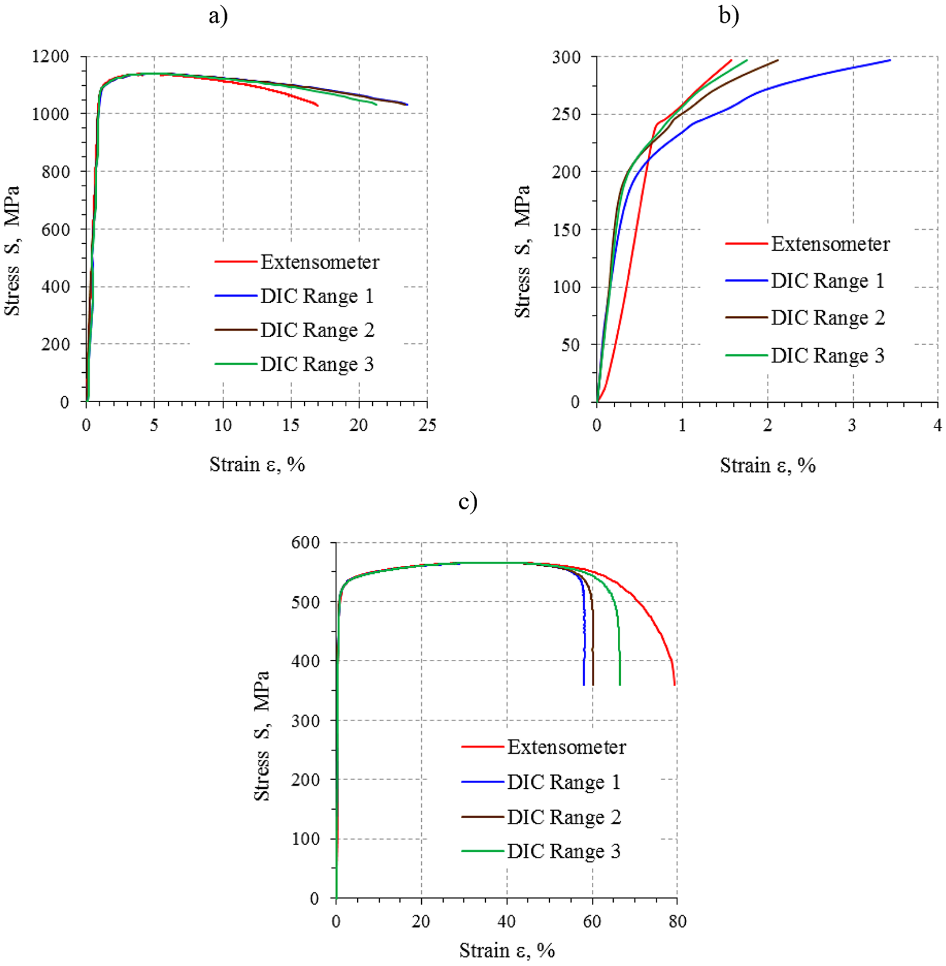

Figure 4. Example of a tensile diagram S = f(ε): a –Ti6Al4V, b – AlSi10Mg, c – 316L

$\sigma_{y0.2}$ = 1085.7 MPa, tensile strength σ_u = 1120.8 MPa, as well as the elongation A = 16.9% values obtained using the extensometer, exhibit lower values compared to the results achieved for the DIC method ($\sigma_{y0.2}$ = 1139.6 MPa, σ_u = 1088.6 ÷ 1096.0 MPa, A = 21.2 ÷ 23.5%). The Young's modulus E reaches the highest value in measurements carried out using an extensometer (E = 119610 MPa). When using an extensometer, the yield point $\sigma_{y0.2}$ = 238.8 MPa and tensile strength σ_u = 297.4 MPa of the AlSi10Mg achieve their highest values. However, the elongation value A = 1.5 % for this measurement method is the lowest. For the measurements conducted using the DIC method, the AlSi10Mg are characterized by yield point $\sigma_{y0.2}$ = 189.9 ÷ 190.7 MPa, tensile strength σ_u = 297.4 MPa, and elongation A = 1.8 ÷ 3.4%

The results obtained for 316L behave in completely different way, with the yield point $\sigma_{y0.2}$ = 484 MPa, tensile strength σ_u = 566.7 MPa, Young's modulus E = 113820 MPa, and elongation A = 79.7% reaching their highest values in the tests conducted with an extensometer. When using the DIC method, the yield point $\sigma_{y0.2}$ = 421 ÷ 433 MPa, the tensile strength σ_u = 566.4 MPa, Young's modulus E = 82042 ÷ 88384 MPa, and elongation A = 58.3 ÷ 66.4%. On the basis of the obtained results, there is an observed relation indicating that as the measurement area decreases in the DIC method, the values of Young's modulus E and elongation A decrease, while the yield point $\sigma_{y0.2}$ increases. An exception was observed in the measurement for 316L, where elongation A increased with the expansion of the measurement area. This might be related to the properties of stainless steel.

MATERIAL HARDNESS

The hardness research was performed on the cross-section obtained from undamaged samples and the samples damaged as a result of

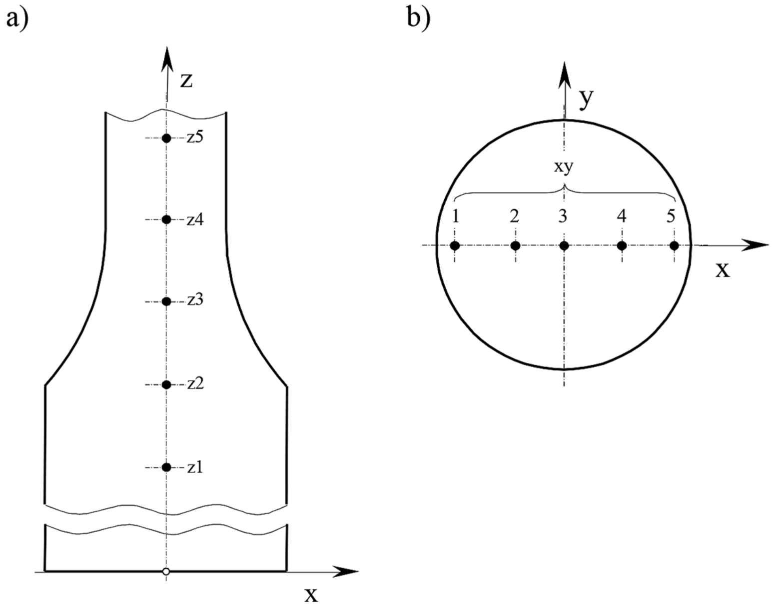

Figure 5. Hardness measurement method: a – schematic presentation of hardness measurements points on the x-z plane x-z, b –schematic presentation of hardness measurements points in the grip section on the x-y plane

a static tensile test: Ti6AL4V, AlSi10Mg, and 316L. The measurements were taken in two planes (in the x-z plane and in the x-y plane) according to the scheme presented in Figure 5. The results of hardness measurements for specimens taken after a static tensile test for three materials are summarized in Table 6. Columns 3, 4 and 5 contain the average hardness values in the x-z plane of the sample, while columns 7, 8 and 9 present the average hardness values obtained in the grip section on the x-y plane. Table 7 presents the results of hardness measurements

Table 6. Vickers HV10 hardness measurement results – loaded samples

No.	Vickers hardness measurement method (HV10)							
	On the x-z plane				On the x-y plane			
	No	Ti6Al4V	AlSi10Mg	316L	No	Ti6Al4V	AlSi10Mg	316L
1	2	3	4	5	6	7	8	9
1	z1	425.5	101.0	242.5	xy1	409.5	105.0	251.0
2	z2	424.5	97.0	241.5	xy2	447.0	116.0	237.5
3	z3	432.0	101.0	239.0	xy3	432.5	121.5	244.0
4	z4	433.0	108.0	342.0	xy4	442.0	122.0	240.0
5	z5	450.5	110.5	360.5	xy5	409.5	101.0	237.5

Table 7. Vickers HV10 hardness measurement results – unloaded samples

No.	Vickers hardness measurement method (HV10)			
	along Z axis			
	No	Ti6Al4V	AlSi10Mg	316L
1	2	3	4	5
1	z1	371.5	118.5	263.0
2	z2	386.0	118.5	259.0
3	z3	383.5	119.0	252.5
4	z4	382.0	117.5	263.0
5	z5	387.0	119.0	249.5

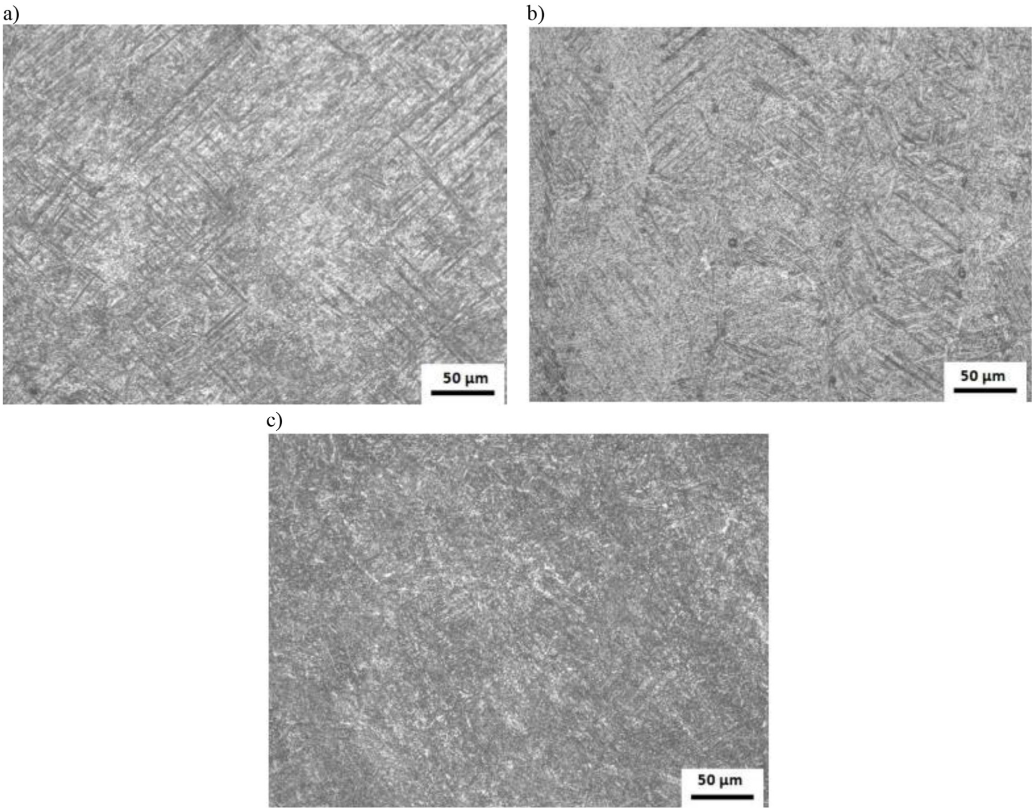

Figure 6. Microstructure of Ti6Al4V, tensile specimen: a – longitudinal section – grip section, b – longitudinal section – reduced section, c – transverse section, MO, etching Kroll's reagent

on the x-z plane for unloaded samples taken from the measuring section.

MATERIAL MICROSTRUCTURE

The microstructure of the Ti6Al4V titanium alloy in a longitudinal sample cross-section is presented in Figure 6a and 6b, while Figure 6c showcases it in a transverse sample cross-section prepared for strength tests. The microstructure observed in Figure 6 is a plate-like structure of the α + β dual-phase alloy. This microstructure consists of alternating plates of α and β phases within the grains of the primary β phase (which are relatively large for dual-phase alloys). In Figure 6a, the microstructure of the grip section does not show any orientation, and the grains are equiaxed. On the longitudinal cross-section of the measurement part (Figure 6b), a directed arrangement of grains in the α + β dual-phase alloy is visible, in accordance with the z axis stretching direction. On the transverse section (Figure 6c), an equiaxed arrangement of lamellar grains of the α + β phase was observed.

Figure 7a shows the AlSi10Mg microstructure on the longitudinal cross-section of the grip section, while Figure 7b presents the longitudinal cross-section of the tensile sample reduced section, and Figure 7c reveals the transverse section of the specimen. Within the grip section of the element (Figure 7a), it was observed that the grains were growing towards the laser print direction along z-axis. On the longitudinal cross-section (Figure 7b), there is a visible growth of grains along the sample's axis in the tension direction (z-axis). In the transverse cross-section of the sample (Figure 7c), the AlSi10Mg alloy grains display a distinct shape typical of eutectic silumin alloys. The microstructure visible in all the images indicates the abundant presence of pores, inclusions, and impurities.

The microstructure of 316L in the longitudinal section of the sample is shown in Figure 8a and 8b. The Figure 8a represents the gripping part, while the Figure 8b describes the reduced section of the specimen after fracturing. Both microstructures in the longitudinal section are characterized by grain orientation along z-axis, which is the direction sample (Figure 8b). In the reduced section of the specimen (Figure 8b), there is a noticeable deformation (elongation) of the grains due to the increasing applied force. There are multiple slip lines present in the microstructure of the stainless steel. Figure 8c shows

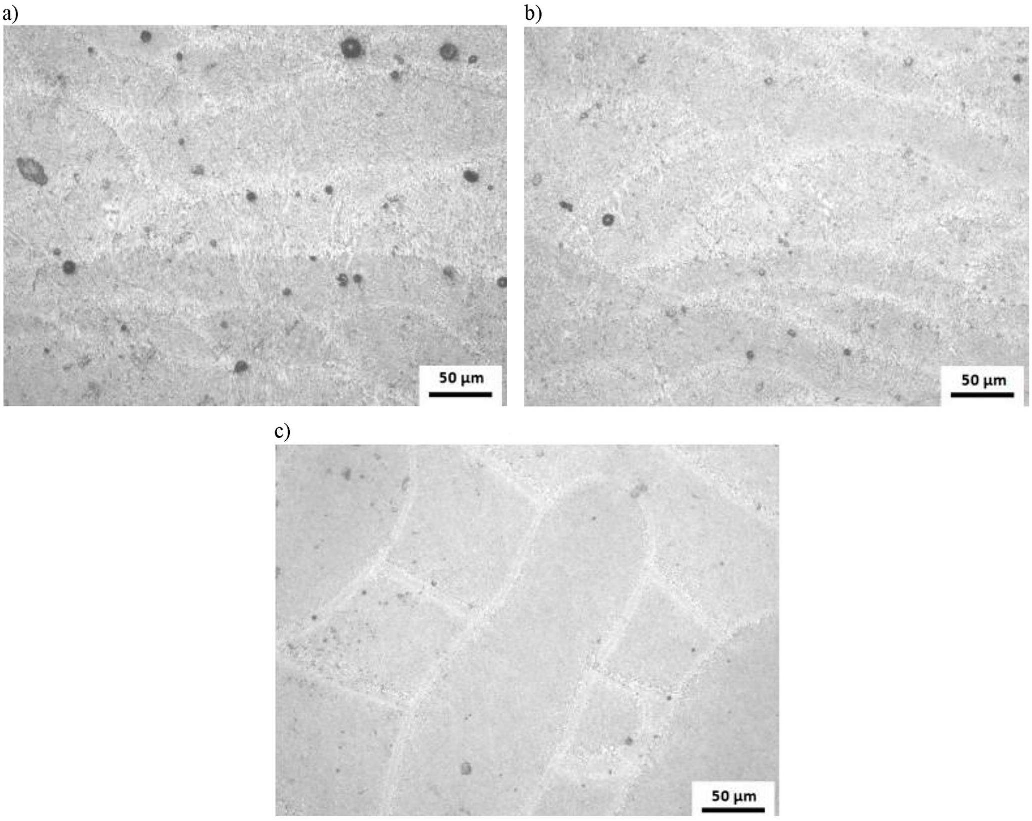

Figure 7. Microstructure of AlSi10Mg: a) longitudinal section – grip section, b) longitudinal section – reduced section, c) transverse section, MO, etching Keller's reagent

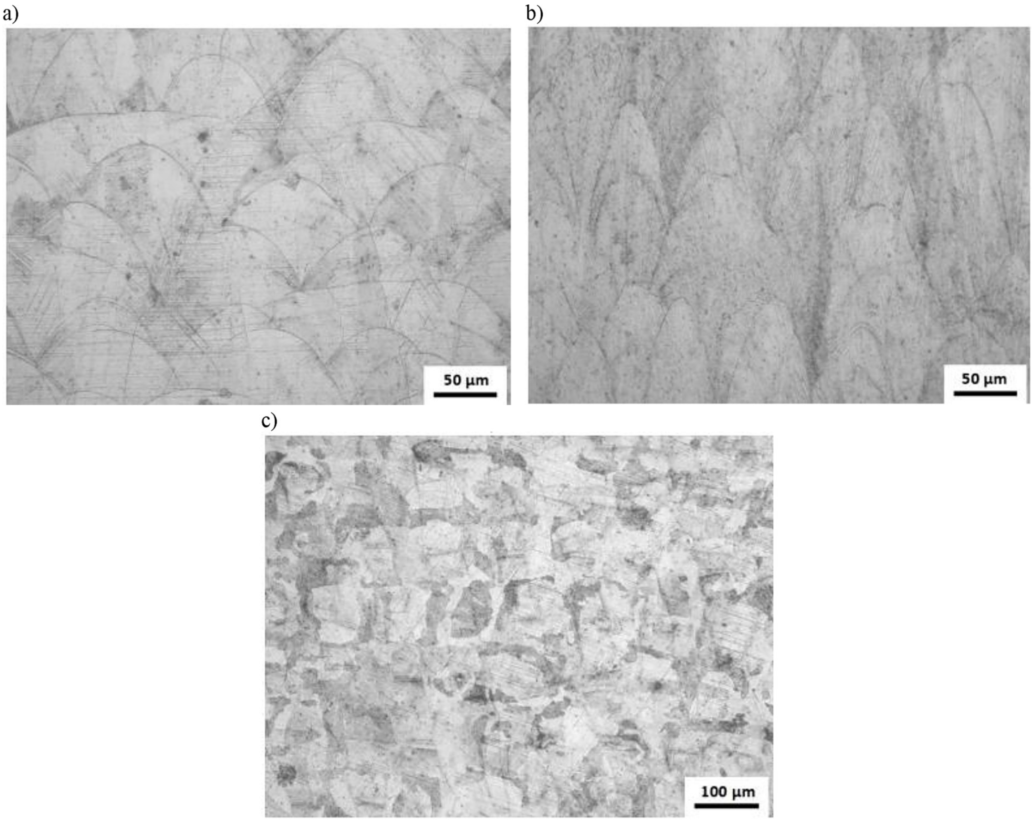

Figure 8. Microstructure of 316L: a) longitudinal section – grip section, b) longitudinal section – reduced section, c) transverse section, MO, etching HCl + HNO_3 + CH_3COOH +$C_3H_8O_3$

the microstructure in the transverse section of the gripping part of 316L steel sample. The equiaxed structure of austenite grains is noticeable. Twin lines, which are typical for austenite, can be observed.

RESEARCH RESULTS ANALYSIS

Analysis of test results under static load conditions

By comparing the measurement results obtained using an extensometer for the Ti6Al4V with the normative parameters (Table 8), it can be seen that the value of the yield point $\sigma_{y0.2}$=1085.7 MPa falls within the specified in the standard range. However, the ultimate tensile strength σ_u =1120.8 MPa is approximately ~ 3.5% lower than the average normative value. In turn, the longitudinal modulus of elasticity E = 119.6 GPa is higher by approximately 14%, and the elongation value A = 16.9% is higher by about ~ 207%. The yield point $S_{y0.2}$ and the ultimate tensile strength S_u for various measurement ranges using digital image correlation DIC are within the ranges given in the standard. Young's modulus for digital image correlation obtained for individual ranges was higher by: ~ 9.8% for L1, ~ 9.5% for L2 and ~ 7.6% for L3. The elongation values obtained exceeded the normative values by: ~ 327.3% for L1, ~ 323.6% for L2, ~ 285.5% for L3.

According to test results, the ultimate tensile strength of AlSi10Mg reaches σ_u = 297.4 MPa, which is about 35% lower than the value specified in the applicable standard. Regarding the yield point, the normative value is $\sigma_{y0.2} = 260 \pm 20$ MPa, which indicates that the results obtained for extensometer measurement ($\sigma_{y0.2}$ = 238.8 MPa) are close to the lower normative range. For the measurement carried out using DIC, the yield point values are considerably lower and fall outside the normative range of $\sigma_{y0.2}$ variability. The Young's modulus obtained for strain measurements using an extensometer is around 14% lower compared to the average normative value. When it comes to DIC digital image correlation, the strain measurement range L1 it is lower about 13%, the range L2 is lower by approximately 25%, and the range L3 is lower by around 29%. Regarding elongation A, the extensometer provided the most deviating value, which was lower by roughly 13.9% compared to the normative value. For the measurements carried out using the DIC method, the range of value changes between 42.8% and 70.7%.

Upon comparing the obtained tensile strength results of 316L steel using strain measurement with an extensometer and DIC with the normative value, it can be concluded that they fall within the acceptable range of variations. The yield point $\sigma_{y0.2}$ obtained from strain measurement using an extensometer is higher by approximately 4.3%, whereas for digital image correlation DIC, it is lower than the normative value in the range from 6.7% to 9.2%. The Young's modulus values achieved as a result of the research are significantly lower than the normative values. The Young's modulus E value for strain measurement using an extensometer is lower by about 32%, and for the DIC method it is lower by 47% to 51% compared to the average value mentioned in the standard. Meanwhile, the value of elongation A obtained using the extensometer is approximately 98.8% higher than that given in the standard. The elongation achieved for digital image correlation is also higher than the normative value: for the L1 range by around 47%, for the L2 range by about 52%, and 66% for the L3 range.

By analyzing all test results and comparing them with normative data for specific materials types, it can be noted that they significantly deviate. These differences are influenced by the additive technology applied in the samples production. Several factors (including laser power, layer thickness of the deposited powder, printing density, etc.), have an impact on the properties of elements made using additive methods, resulting in modification to the mechanical properties of the material.

By comparing the research results obtained through DIC strain measurement with the results achieved using an extensometer, it can be observed that higher Young's modulus values reached the measurements for the Ti6Al4V alloy (Fig. 9a) and 316L steel (Fig. 9c), using an extensometer (measuring range L4 = 10 mm). For the titanium alloy Ti6Al4V, the percentage differences in the range of the E modulus (Fig. 9a) amount 3.6% to 5.6%. For the 316L stainless steel, percentage differences in values of the Young's modulus (Fig. 9c) range from 22.3% to 27.9%. Considering the AlSi10Mg aluminum alloy, the Young's modulus values (Fig. 9b) obtained for L1 = 1.36 mm and L4 = 10 mm are similar, with a difference in the results less than 1%. The E modulus values for L2

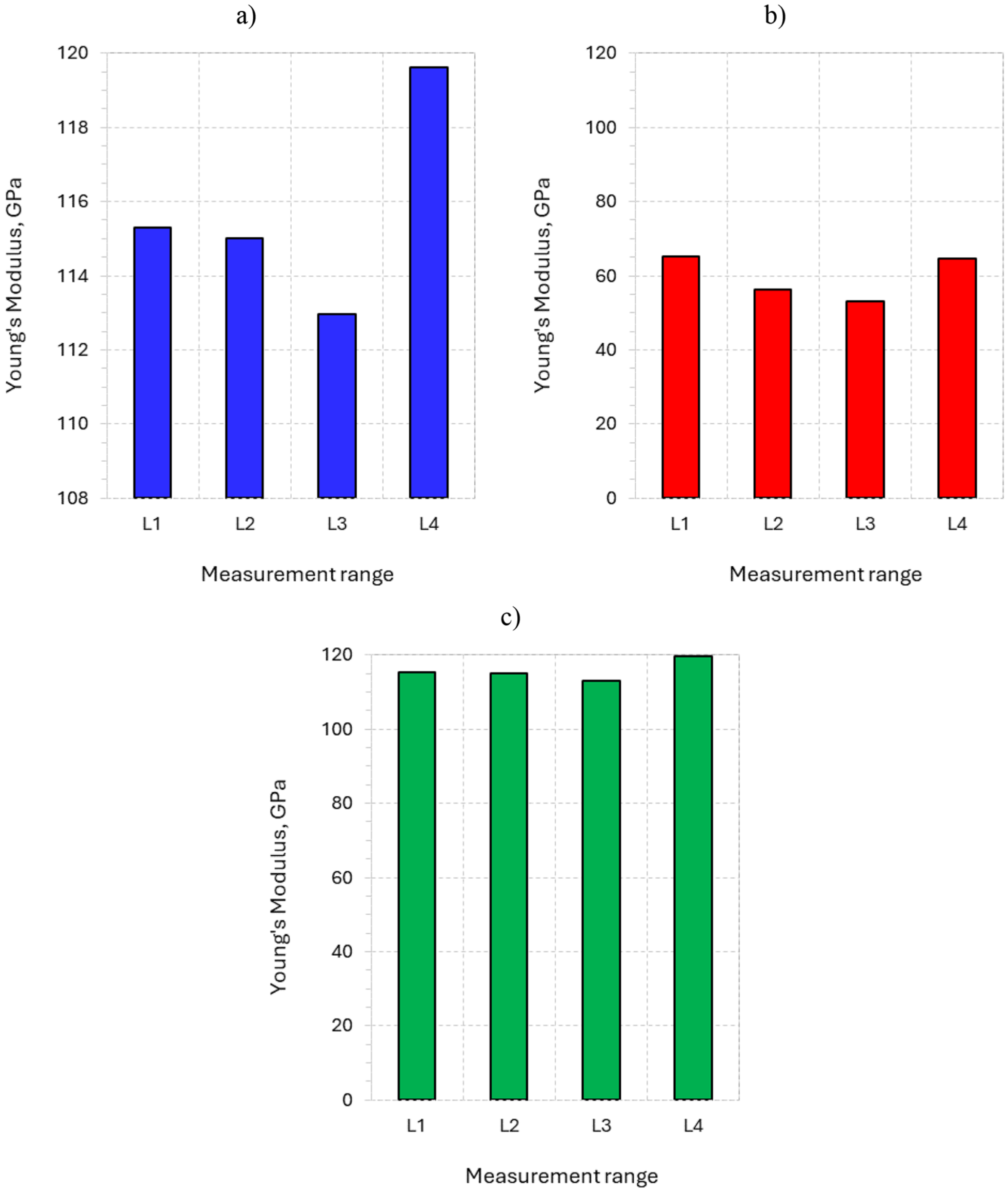

Figure 9. Diagram of changes in the Young's modulus value for different strain measurement ranges: a – Ti6Al4V, b – AlSi10Mg, c – 316L

= 2.72 mm and L3 = 3.49 mm are lower by approximatley 12.7% and 18.0%, respectively.

Changes in the Young's modulus values for individual measurement ranges in samples may be related to local changes in material properties. Individual measurement bases include small fragments of the sample in the area of the greatest deformations and subsequent cracking. This causes the greatest local changes in material properties to occur in this area. The difference in the Young's modulus values may result from the inaccuracy of the digital image correlation method. When analyzing the test results, it can be concluded that the DIC method is not a reliable method compared to the extensometer method commonly used in engineering tests. In the case of the Ti6Al4V, AlSi10Mg and 316L samples, the Young's modulus E value decreases with the increase in the area L subjected to analysis. This may result from poor lighting of the sample during the tests (too dark or overexposed photos), which translates into the program "losing" points during the analysis. It can be seen that with the smallest area, there may be fewer such errors and the modulus value from the smallest range is similar to the value obtained using an extensometer.

The differences in the Young's modulus values for AlSi10Mg may result from weaker surface adhesion of the material between some of the applied layers, which translates into their delamination and interlayer cracking (aluminium is a difficult-to-weld material). In the case of area L1, which is the smallest fragment subjected to analysis, the sample cracked as a result of tensile forces and the greatest changes in the microstructure of the material occurred, which translated into obtaining a Young's modulus value similar to the traditional method using an extensometer. As the measurement range increased, areas with smaller displacement values appeared (not including only the sample crack site). The average strain value in areas L2 and L1 was lower than in the case of the L3 measurement range. The largest measurement range L4 corresponds to the extensometer range and was characterized by the lowest strain value.

During the analysis of the elongation measurement results for tested materials (Fig. 10), it was noticed that the elongation value A decreases as the measurement base increases for both Ti6Al4V (Fig. 10a) and AlSi10Mg (Fig. 10b). The highest values are given for L1 = 1.36 mm, and the lowest for the value for L4 = 10 mm. When it comes to 316L (Fig. 10c), an increase in the elongation A can be seen as the strain measurement base expands from L1 to L4. It is assumed that the change in the elongation value is related to the properties of the material, including its chemical composition and crystalline structure.

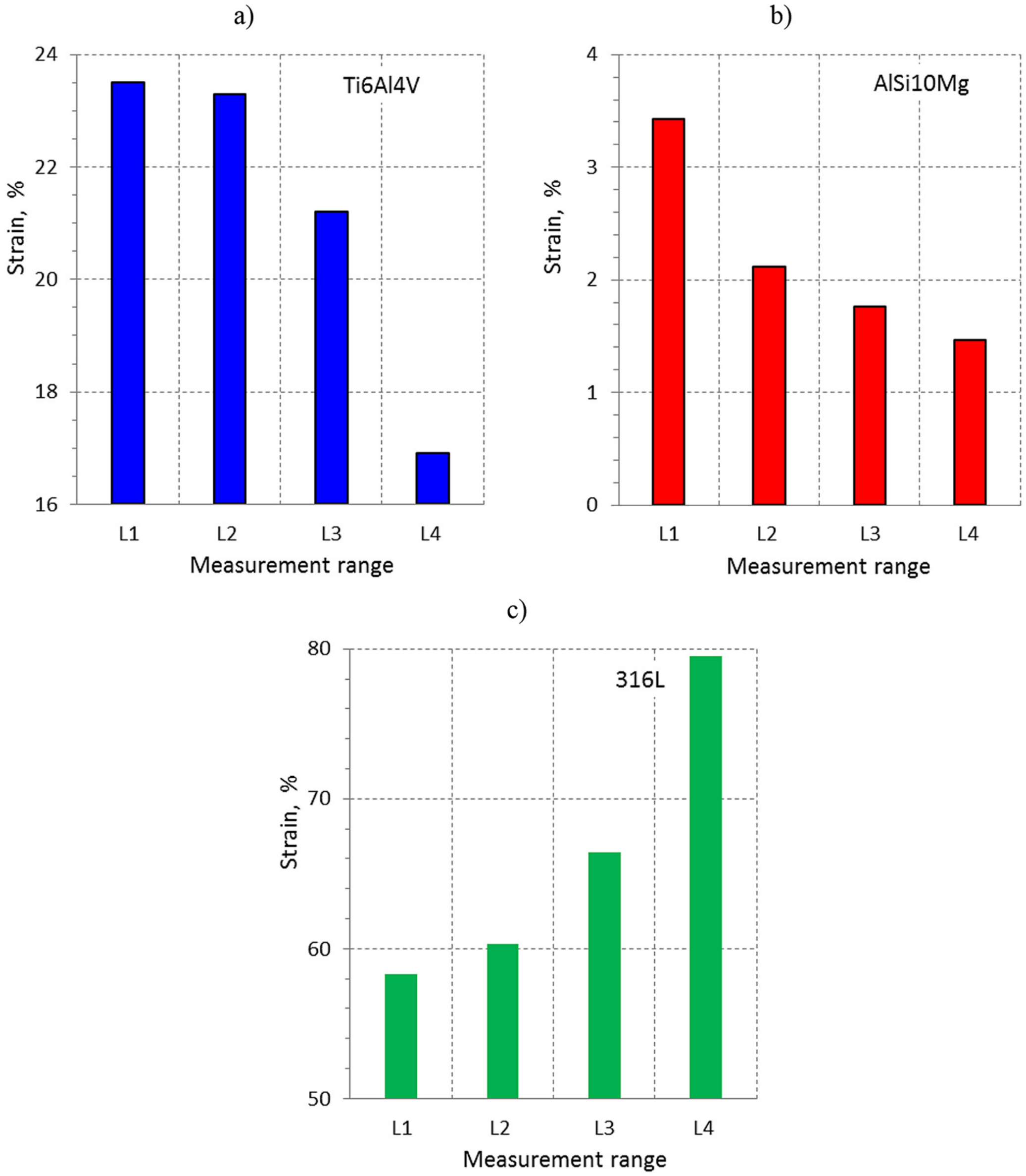

Figure 10. Diagram of changes in the elongation value of material for different strain measurement ranges: a – Ti6Al4V, b – AlSi10Mg, c – 316L

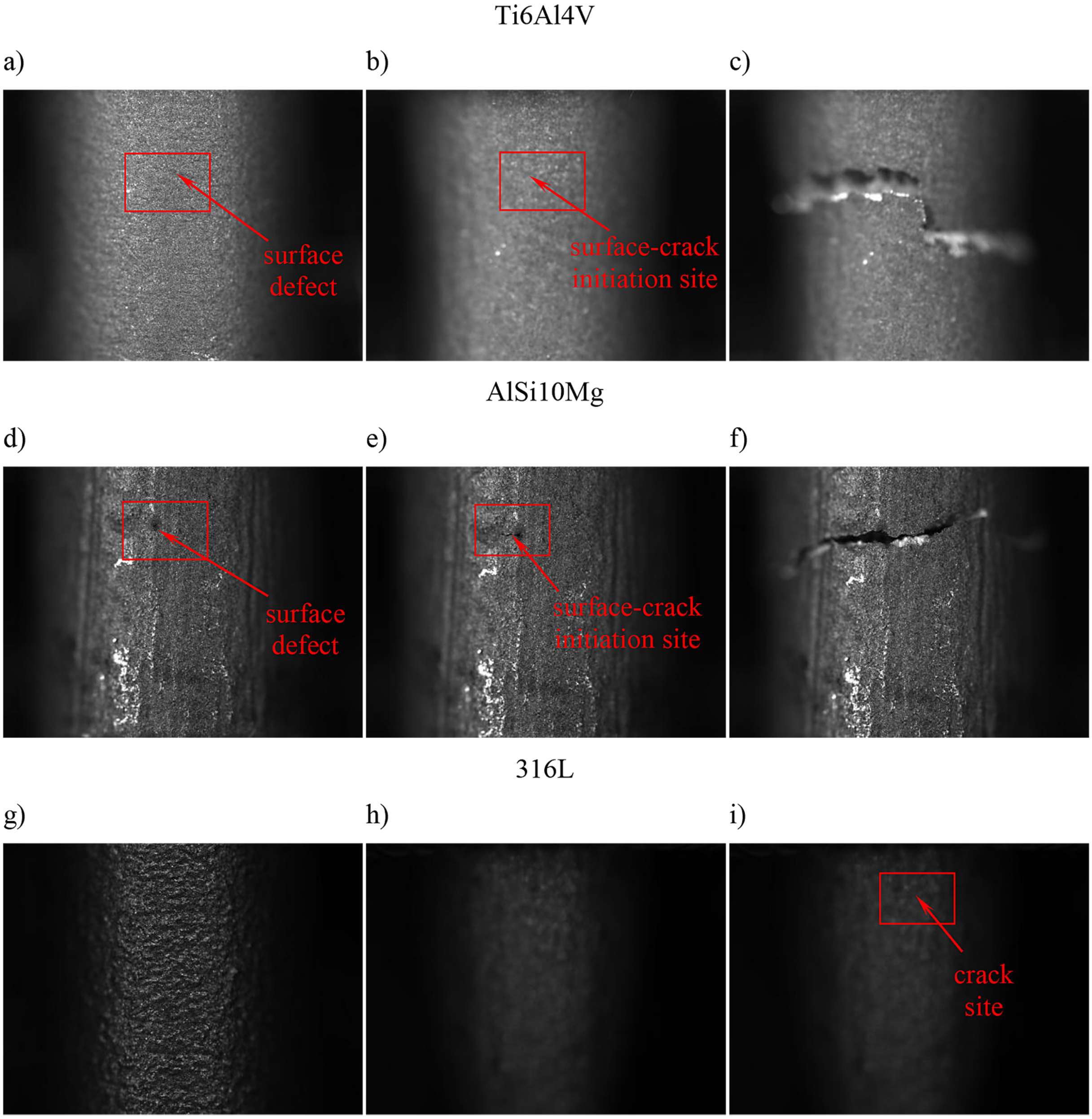

Figure 11. Photos taken during the static tensile test using a BASLER acA4024-8gm camera: a, d, g – reference image, b, e, h – last recorded image before failure, c, f, i – image recorded immediately after sample breaking

Strain analysis based on the DIC method

The data obtained based on digital image correlation during tensile test allowed for the analysis of local deformations occurring in the tested samples. Figure 11 presents images of the measurement area of the specimen, which were used for the analysis. Figure 11a, b and c portray a sample of Ti6Al4V. Figure 11d, e, f shows a fragment of a sample of AlSi10Mg, while Figure 11g, h, and present a sample of 316L. Figures 11a, d, and g present the reference images recorded at the beginning of the stength test.

In the case of Ti6Al4V and AlSi10Mg, there are specific surface defects that exhibit crack formation due to tensile forces. Figure 11b highlights the initiation of a crack from the site of a surface defect. A comparable trend is observed for the AlSi10Mg specimen (Fig. 11e) – crack initiation occurred at the site of porosity formation. The fractures of the aluminum alloy and titanium alloy specimens indicate the brittle nature of cracking forming along successive deposited layers. This may indicate weak interlayer bonds resulting from the additive manufacturing process. Due to

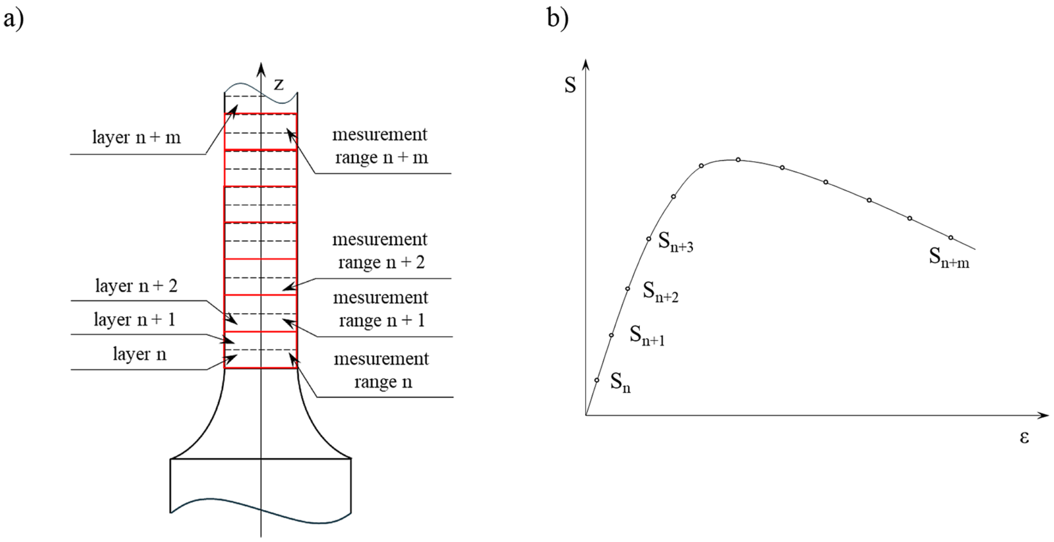

Figure 12. Schematic illustration of: (a) analyzed measurement areas, (b) stress levels at which strain values were measured

the plasticity of the 316L material, a visible sample crack is not apparent in the photos.

On the basis of the analysis of the images in Figure 11, local strain values were determined for the smallest fragment possible to analyze – 2 layers. Figure 12a schematically shows the sintered layers that make up the entire sample. Two adjacent layers were defined as the measurement range. For each of the presented measurement ranges, a tensile diagram was created in accordance with Figure 12b. For specific stress values S_{n+m}, strain values were read for each measurement range. Table 8 lists the stress values for which the strain values were read in a given measurement range. This allowed for the development of graphs of deformation changes depending on the measurement range for the tested materials: Ti6Al4V (Fig. 13), AlSi10Mg (Fig. 14) and 316 L (Fig. 15). These graphs show local deformations and help determine where the crack initiated in the sample. On the basis of the analysis of images presented in Figure 11, local strain values were determined for the tested materials. The

Table 8. Stress values corresponding to the measured strain values

Stress designation in relation to the tension diagram (Fig. 12b)	Stress [MPa]		
	Ti6Al4V	AlSi10Mg	316L
S_1	54.,2	61.4	534.6
S_2	983.5	165.5	547.2
S_3	112.7.3	213.9	553.0
S_4	1139.6	221.1	557.8
S_5	1131.5	231.4	561.0
S_6	1118.2	245.6	563.2
S_7	1099.9	259.5	565.0
S_8	1064.3	272.5	565.9
S_9	1038.0		566.1
S_{10}			566.2
S_{11}			564.7
S_{12}			562.0
S_{13}			557.6
S_{14}			547.6
S_{15}			527.5
S_{16}			492.5

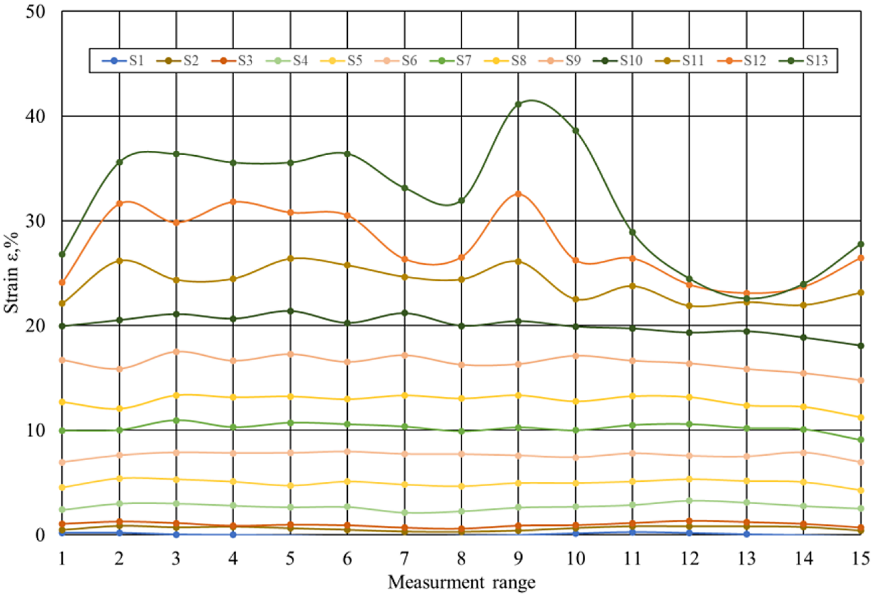

Figure 13. Graph of strains changes in AlSi10Mg in individual measurement ranges (2 layers) with increasing stress value

DIC method allowed for determining the smallest possible area of the sample to be analyzed, which included two layers of the deposited material. Figure 12a shows adjacent layers, which make up the measurement ranges from the first to the last, while Figure 12b shows the stress-strain diagram for individual measurement ranges. The sintered layers marked in Figure 12a, e.g. layer n and layer n+1, made up the first measurement range 1. The next two adjacent layers were defined as the next measurement range. For each measurement range (1–15 for Ti6Al4V, 1–14 for AlSi10Mg and 1–15 for 316L) – two adjacent layers, a separate stress-strain diagram was obtained. Then, based on the obtained graphs, the strain values were read from them for specific stress values (Fig. 12b) from Sn to Sn+m, and the read values were entered into Table 8. This allowed for the development of graphs of strain changes depending on the measurement range for the tested materials: titanium alloy Ti6Al4V (Fig. 13), aluminum alloy AlSi10Mg (Fig. 14) and steel 316 L (Fig. 15). Figures 13–15

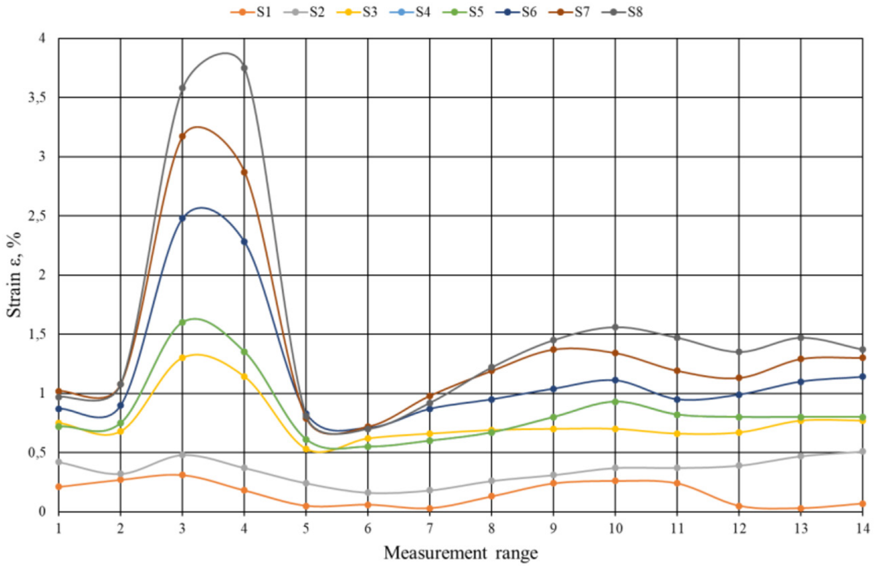

Figure 14. Graph of strains changes in AlSi10Mg in individual measurement ranges (2 layers) with increasing stress value

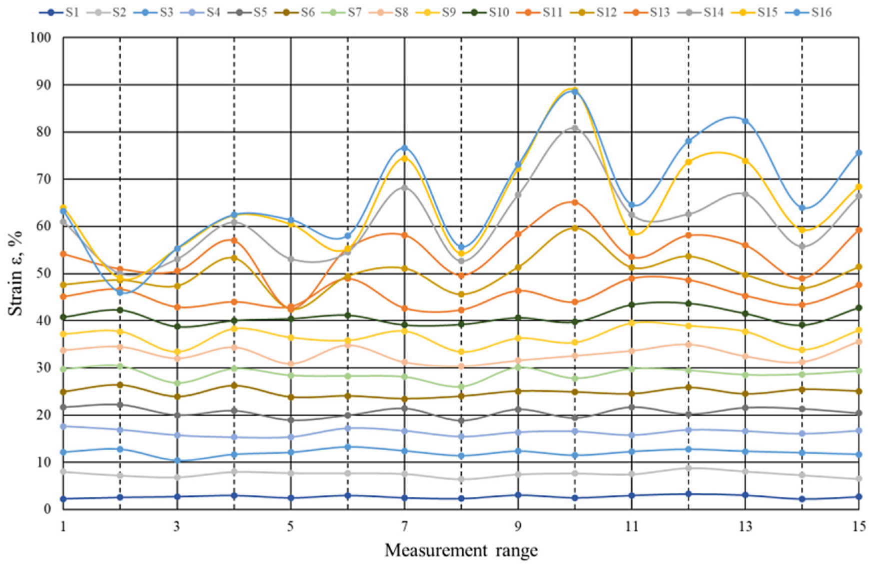

Figure 15. Graph of strains changes in 316L in individual measurement ranges (2 layers) with increasing stress value

present graphs on which the numbers of the measurement ranges in accordance with Fig. 12a are placed on the horizontal axis. On the other hand, the strain in %, read from the tension graph of a given pair of adjacent layers, is presented on the vertical axis. These graphs present local strains and allow for determining the place in the sample where the crack initiation occurred.

According to the analysis of the chart in Figure 13 for the Ti6Al4V samples, the deformation changes in the layers until reaching stress $S_4 = \sigma_u = 1139.6$ MPa are characterized by slight changes. It can be observed that they occur uniformly distributed across the entire measured length of the sample. After reaching the temporary tensile strength, differences in the deformation of individual layers are observed in the sample. The highest strain value is achieved in area 6, where the sample fracture occurred. Meanwhile, the lowest defformation is observed in area 3.

The data for 316L stainless steel is presented in the chart in Figure 14. When analyzing the changes in local strains, it can be seen that at a stress $S_3 = 213.9$ MPa, there is a noticable increase in deformations in zones 3 and 4, which progressively grows with increasing stress values. The indicated range is located in the area of sample's crack. This could suggest the formation of a crack on the sample's surface at the stress S_3. The areas next to the crack, 1 and 2, as well as 5 and 6, demonstrate the lowest local deformation values. The strain values in the rest of the layers change evenly, reaching approximately 1.5% at the tensile strength $S_8 = 272.5$ MPa.

The changes in local deforamtion for each layer in the measurement section of the 316L stainless steal specimen are presented in graph in Figure 15. The presented data indicate that in each layer, deformations reach similar values within the range of 40% up to stress levels near $\sigma_u = 566.7$ MPa. After exceeding σ_u, an increase in strain is observed in selected layers. A significant growth in deformation is observed within the 10th measurement range, ranging from 43.97% for S_{11} to 59.65 for S_{12}. This layer has the highest local deformation value of 88.47%. This may be related to the progressive delamination of the layers, eventually causing the complete failure of the specimen.

Comparison of hardness test results

On the basis of the conducted research, hardness variation charts (Fig. 12) have been prepared for the x-z plane and the x-y plane of the sample.

Regarding the Ti6Al4V, the hardness results on the x-z plane show an increasing trend and are within the range of 425.5 ÷ 450.5 HV10. According to the measurement scheme (Fig. 5a), the first measurement point is located in the gripping part of the sample, while the last measurement point is closest to the sample's fracture edge. For the Ti6Al4V sample, it can be observed that the hardness on the x-z plane increases as it approaches the crack point. The rise in hardness at the fracture site may be related to the deformations occurring in this area due to the static tensile test. Comparing the hardness results achieved for the sample after a static tensile test with those obtained for the specimen not subjected to a load, it can be seen that the hardness for the loaded sample is higher in the range of 28.5 ÷ 63.5 HV10. An increase in hardness may indicate changes in the material structure caused by the tensile force.

Figure 12b illustrates the hardness points in the grip part of the Ti6Al4V sample on the x-y plane after the tensile test. The measurement was performed based on the scheme presented in Figure 5b. The hardness value range varies from 409.5 to 447 HV10, indicating changes in hardness across the cross-section of the sample of 37.5 HV10. The hardness results obtained for the cross-section area of the sample (x-y plane) are similar to the values measured on the x-z plane. The difference between the highest and lowest results is 41 HV10.

The hardness measurement of the AlSi10Mg specimens was carried out in the same manner as the analysis of the Ti6Al4V samples. The range of hardness value changes for the aluminum alloy samples on the x-z plane falls within 97 to 110.5 HV10, indicating slight variations within a range of 13.5 HV10 (Figure 16). The initial measurement point is located in the grip section of the sample, while the final measurement point is closest to the specimen's fracture edge. The impact of plastic deformations caused by sample stretching on the hardness cannot be determined. This may be related to small strain values (locally ε ≈ 4%) and brittle fracture of the sample. The results of hardness measurements on the x-z plane for the unloaded sample are 117.5 to 119 HV10. One of the measurements differs from the others by 22 to 24 HV10. This could be related to the measurement being taken at the grain boundary. The achieved results are higher than those obtained for the same plane, but for the samples subjected to a static tensile test. This may indicate that the tensile force influenced a change in the microstructure, leading to decrease in the material hardness. The hardness measurement in the grip section of the sample on the x-y plane following the tensile test indicates a range of value between 101 and 121.5 HV10. This proves minimal changes in hardness in the transverse cross-section of the sample, which amounts to 20.5 HV10. The hardness results obtained for the cross-section of the sample (x-y plane) are close to the values measured on the x-z plane. The difference between the extreme results is 25 HV10.

The range of hardness value changes for 316L after a static tensile test on the x-z plane is between 239 and 360.5 HV10. The first measurement point is in the grip section of the specimen (242.5 HV10), whereas the last measurement point is closest to the sample's fracture edge (360.5 HV10). The distribution of hardness results indicates the impact of plastic deformations resulting from the tensile test on hardness. With the increase in strain values (locally ε ≈ 58%), the material hardness also increases. The hardness results for the same plane, but for unloaded samples, range from 249.5 to 263 HV10. Hardness measurement in the gripping part of the sample

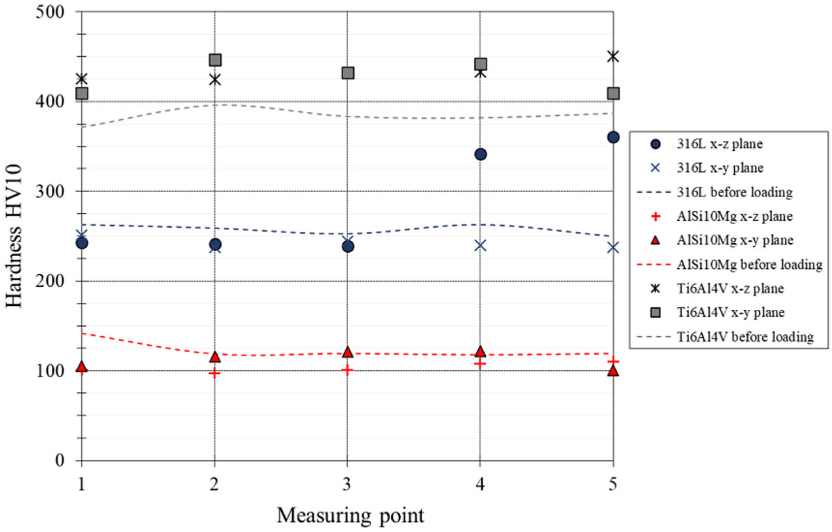

Figure 16. The HV10 hardness distribution in the analyzed samples

on the x-y plane after the tensile test indicates that the changes in values are in the range of 237.5 to 251 HV10, which suggests slight hardness variations of the sample amounting to 13.5 HV10.

The hardness results obtained for the cross-section of the sample (x-z plane) after the static tensile test differ from the values measured on the same plane for unloaded samples. The hardness results for the x-y plane do not show significantly differences compared to the results gain for the x-z plane. The hardness results for Ti6Al4V and 316L on the x-z plane, measured in the highly strained section due to stretching (point no. 4 and no. 5), are higher than the rest of the measurements obtained.

The hardness test results for the samples subjected to a static tensile test show an increase in the average hardness value compared to the unloaded samples in the case of Ti6Al4V by 51.1 HV10. In the case of the 316 L steel, a significant increase in hardness compared to the results obtained for the unloaded sample occurs in the area of the greatest plastic deformations. On the other hand, for AlSi10Mg, the static tensile test reduced the average hardness value by 15 HV10 compared to the unloaded samples.

CONCLUSIONS

The study presents the results of research under static load conditions regarding three types of materials commonly used in the production of machine components using additive technology. The mechanical properties (strength) of the specimens with standard dimensions made by additive manufacturing were compared to the mechanical properties of samples made by classical methods (according to standards). In all cases, tensile tests indicated that the tensile strength of samples made using the additive manufacturing is comparable to or higher than that of conventional samples. Only for aluminum samples there is no defined standard value of mechanical properties for classic manufacturing techniques. Differences between the obtained results of mechanical properties and the normative values for conventional methods may result from the influence of the use of additive technology in the production of samples. The properties of elements made using additive methods are influenced by several factors (including laser power, thickness of the deposited powder layer, print density, etc.), which causes modification of the mechanical properties of the material.

The strength tests carried out using DIC indicated a relationship related to the reduction of the measuring range area. With the reduction of the measuring area, the values of Young's modulus E and elongation A decrease, while the yield strength $\sigma_{y0.2}$ increases. Young's modulus, which is a material constant, should have the same value for each of the measurement methods used. Changes in the values of Young's modulus for individual measuring ranges in the samples may be related to locally occurring changes in the material properties. Moreover, in the case of an aluminum alloy, the discrepancies in the obtained values of Young's modulus may be related to the formation of weak interlayer bonds (adhesion) in the laser melting process and the associated occurrence of local deformations at the weakest bond location. It is also assumed that the occurring changes in the elongation values were related to the material properties, including its chemical composition and crystal structure. In the case of Ti6Al4V and AlSi10Mg, surface defects were observed, where cracks developed as a result of the action of tensile forces. The fractures of the aluminum alloy and titanium alloy samples showed a brittle nature of the crack, which occurred along the successive layers deposited. This also indicates weak interlayer bonds resulting from the additive manufacturing process.

Microstructural tests have shown that in the grip part of the sample, the microstructure visible in the longitudinal cross-sections for ALSi10Mg and 316L is characterized by a directional grain pattern. This direction is consistent with the printing direction, i.e. along the z axis of the stretched samples. The directional microstructure produced by printing methods can cause anisotropy of strength properties and their increase along the z axis of the sample. Material hardness tests indicated an increase in hardness resulting from the static tensile test for two of the tested materials: Ti6Al4V and 316 L. The AlSi10Mg aluminum alloy was characterized by a decrease in hardness due to the action of tensile forces. The obtained test results can be used to determine the tensile strength using non-destructive tests.

On the basis of the strength tests conducted, micro fractographic analysis of sample fractures, and detailed analysis of the above-mentioned tests, it can be concluded that elements made by the use of additive manufacturing can, in the majority of cases, serve as substitutes for structural elements manufactured using conventional methods (reduction methods – e.g. cutting, turning, or non-reduction methods – drawing, plastic deformation, etc.). These findings are supported by the conducted strength tests carried out on additive and classic normative samples. The basic condition is that the direction of the load corresponds to the direction of layer formation in the additively manufactured structural component. The use of additive (incremental) methods in the production of structural elements and entire mechanical devices brings many advantages, such as the speed of production of the finished structural element, reducing operations and procedures in the manufacturing process, cost savings (economics), and more.

REFERENCES

1. Agius, D., et al., A review of the as-built SLM Ti-6Al-4V mechanical properties towards achieving fatigue resistant designs. Metals, 2018, 8, 75.
2. Buchbinder D., et al., High power selective laser melting (HP SLM) of aluminum parts., Physics Procedia, 2011, 12(1), 271–278.
3. Duda T., Raghavan L. V., 3D Metal Printing Technology, IFAC-Papers On Line, 2016, 49(29), 103–110.
4. Ford S.L.N., Additive Manufacturing Technology: Potential Implications for U.S. Manufacturing Competitiveness, Journal of International Commerce, Economics and Policy, 6, 2014, 40.
5. Kruth J.P., et al., Binding mechanisms in selective laser sintering and selective laser melting. Rapid Prototyp, 2005, 11, 26–36.
6. Weißmann V., et al, Influence of the structural orientation on the mechanical properties of selective laser melted Ti6Al4V open-porous scaffolds. Materials & Design, 2006, 95, 188–197.
7. Shipley H., et al., Optimisation of process parameters to address fundamental challenges during selective laser melting of Ti-6Al-4V: A review, International Journal of Machine Tools and Manufacture, 2008, 128, 1–20.
8. Rafi H., Starr T., Stucker B., A comparison of the tensile, fatigue, and fracture behavior of Ti–6Al–4V and 15-5 PH stainless steel parts made by selective laser melting, International Journal of Advanced Manufacturing Technology, 2013, 69, 1299–1309.
9. Gong H., et al., Influence of defects on mechanical properties of Ti-6Al-4V components produced by selective laser melting and electron beam melting, Materials and Design, 2015, 86, 545–554.
10. Kempen K., et al., Microstructure and mechanical properties of selective laser melted 18Ni-300 steel, Physics Procedia, 2012, 12(1), 255–263
11. Casalino G., et al., Experimental investigation and statistical optimisation of the selective laser melting process of a maraging steel, Optics and Laser Technology, 2015, 65, 151–158.
12. Shipley H., et al., Optimisation of process parameters to address fundamental challenges during selective laser melting of Ti-6Al-4V: A review, International Journal of Machine Tools and Manufacture, 2008, 128, 1–20.
13. Han J., et al., Microstructure and mechanical property of selective laser melted Ti6Al4V dependence on laser energy density, Rapid Prototyping Journal, 2017, 23(2), 217–226.
14. Hagedorn-Hansen D., et al., The effect of selective laser melting scan strategies on deviation of hybrid parts, South African Journal of Industrial Engineering, 2020, 28(3), 200–212.
15. Smith D., et al., Microstructure and mechanical behavior of direct metal laser sintered Inconel alloy 718, Materials Characterization, 2016, 113, 1–9.
16. Kempen K., et al., Lowering thermal gradients in Selective Laser melting by pre-heating the baseplate, Solid Freeform Fabrication Proceedings, 24, 2013.
17. Kumar P., Prakash O., Ramamurty U., Micro-and meso-structures and their influence on mechanical properties of selectively laser melted Ti-6Al-4V, Acta Materialia, 2018, 154, 246–260.
18. Leicht A., et al., Effect of scan rotation on the microstructure development and mechanical properties of 316L partsproduced by laser powder bed fusion, Materials Characterization, 2020, 163, 110309.
19. Agius, D., Kourousis, K.I., Wallbrink, C., A Review of the As-Built SLM Ti-6Al-4V Mechanical Properties towards Achieving Fatigue Resistant Designs. Metals, 2018, 8, 75.
20. Nickel A., Barnett D., Prinz F., Thermal stresses and deposition patterns in layered manufacturing, Materials Science and Engineering: A, 2001, 317, 59–64.
21. Bian P., et al., Influence of laser power and scanning strategy on residual stress distribution in additively manufactured 316L steel, Optics and Laser Technology, 2020, 132, 106477.
22. Acevedo R., et al., Residual stress analysis of additive manufacturing of metallic parts using ultrasonic waves: State of the art review, Journal of Materials Research and Technology, 2020, 9(4), 9457–9477.
23. Benedetti M., et al., Low and high-cycle fatigue resistance of Ti-6Al-4V ELI additively manufactured via selective laser melting: Mean stress and defect sensitivity, International Journal of Fatigue, 2018,107, 96–109.

24. Triantaphyllou A., et al., Surface texture measurement for additive manufacturing, Surface Topography: Metrology and Properties, 2015, 3(2), 24002.
25. Riemer A., et al., On the fatigue crack growth behavior in 316L stainless steel manufactured by selective laser melting, Engineering Fracture Mechanics, 2014, 120, 15–25.
26. Ren S., Chen Y., Liu T., Qu Xuanhui, Effect of build orientation on mechanical properties and microstructure of Ti-6Al-4V manufactured by selective laser melting, metallurgical and materials transactions A, 2019, 50, 4388–4409.
27. Chandramohan P., Bhero S., Obadele B., Olubambi P., Ravisankar B., Effect of built orientation on direct metal laser sintering of TI-6AL-4V, Indian Journal of Engineering and Materials Sciences, 2018, 25(1), 69–77.
28. Mower T., Long M., Mechanical behavior of additive manufactured powered-bed laser-fused materials, Materials Science & Engineering A, 2016, 651, 198–213.
29. Beretta S., Romano S., A comparison of fatigue strength sensitivity to defects for materials manufactured by AM or traditional processes, International Journal of Fatigue, 2017, 94, 178–19.
30. Buchbinder D., Schleifenbaum H., Heidrich S., Meiners W. Bültmann, J., High power Selective Laser Melting (HP SLM) of aluminum parts, Physics Procedia, 2011, 12(1), 271–278.
31. Wang Z., Palmer T., Beese A., Effect of processing parameters on microstructure and tensile properties of austenitic stainless steel 304L made by directed energy deposition additive manufacturing, Acta Materialia, 2016, 110, 226–235.
32. Luo C., Zhang Y., Effect of printing orientation on anisotropic properties in resistance spot welded 316L stainless steels via selective laser melting, Materials Letters, 2019, 254, 237–241.
33. Liu S., Li H., Qin C., Zong R., Fang X., The effect of energy density on texture and mechanical anisotropy in selective laser melted Inconel 718, Materials & Design, 2020, 191, 108642.
34. Witkin D., Patel D., Albright T., Bean G., McLouth T., Influence of surface conditions and specimen orientation on high cycle fatigue properties of Inconel 718 prepared by laser powder bed fusion, International Journal of Fatigue, 2020, 132, 105392.
35. Brookes K., Maraging steel for additive manufacturing, Metal Powder Report, 2016, 71(3), 149–152.
36. Yao Y., et al., Microstructural heterogeneity and mechanical anisotropy of 18Ni-330 maraging steel fabricated by selective laser melting: The effect of build orientation and height, Journal of Materials Research, 2020, 35(15), 2065–2076.
37. Kang L., et al., Experimental study of mechanical properties of laser additively manufactured 316L stainless steels, Structures, 2023, 54, 221–235.
38. Falkowska A., Seweryn A., Fatigue life of 316L steel sinters of varying porosity under condition of uniaxial periodically variable loading at a fixed stress amplitude, International Journal of Fatigue, 2018, 117, 496–510.
39. Guan K., et al., Effects of processing parameters on tensile properties of selective laser melted stainless steel, Materials & Design, 2013, 50, 581–586.
40. Salman O., et al., Effect of heat treatment on microstructure and mechanical properties of 316L steel synthesized by selective laser melting, 2019, 748, 205–212.
41. Mei X., et al., Interfacial characterization and mechanical properties of 316L stainless steel/Inconel 718 manufactured by selective laser melting, Materials Science & Engineering A, 2019, 758, 185–191.
42. Zhong T., et al., Mechanical properties of lightweight 316L stainless steel lattice structures fabricated by selective laser melting, Materials & Design, 2019, 181, 108076.
43. Read N., et al., Selective laser melting of AlSi10Mg alloy: Process optimization and mechanical properties development, Materials & Design, 2015, 65, 417–424.
44. Anwar A., Pham Q., Selective laser melting of AlSi10Mg: Effects of scan direction, part placement and inert gas flow velocity on tensile strength, Journal of Materials Processing Technology, 2017, 240, 388–396.
45. Mfusi B., et al., The effect of selective laser melting build orientation on the mechanical properties of AlSi10Mg parts, IOP Conf. Series: Materials Science and Engineering, 2018, 430, 012028.
46. Dong Z., et al., Orientation dependency for microstructure, geometric accuracy and mechanical properties of selective laser melting AlSi10Mg lattices, Journal of Alloys and Compounds, 2019, 791, 490e500.
47. Zhang Ch., et al., A comparative study on single-laser and multi-laser selective laser melting AlSi10Mg: defects, microstructure and mechanical properties, Materials Science & Engineering A, 2019, 746, 416–423.
48. Yakout M., Elbestawi M., Veldhuis S., A study of the relationship between thermal expansion and residual stresses in selective laser melting of Ti6Al-4V, Journal of Manufacturing Processes, 2020, 52, 181.
49. Yan X., et al., Effect of heat treatment on the phase transformation and mechanical properties of Ti6Al4V fabricated by selective laser melting, Journal of Alloys and Compounds, 2018, 764, 1056–1071.
50. Benedetti M., Cazzolli M., Fontanari V., Leoni M., Fatigue limit of Ti6Al4V alloy produced by Selective Laser Sintering, 21st European Conference on Fracture in Catania, Procedia Structural Integrity, 2016, 2, 3158–3167.
51. Kasperovich G., Hausmann J., Improvement of

fatigue resistance and ductility of TiAl6V4 processed by selective laser melting, Journal of Materials Processing Technology, 2015, 220, 202–214.

52. ASTM F2924-14 Standard Specification for Additive Manufacturing Titanium-6 Aluminum-4 Vanadium with Powder Bed Fusion
53. Mouritz A., Introduction to Aerospace Woodhead Publishing Limited, 2012.
54. Beibei H., et al., Microstructural characteristic and mechanical property of Ti6Al4V alloy fabricated by selective laser melting, Vacuum, 2020, 150, 79–83.
55. Benedetti M., Torresani E., Leoni M., Fontanari V., Bandini M., Pederzolli C., Potrich C., The effect of post-sintering treatments on the fatigue and biological behavior of Ti-6Al-4V ELI parts made by selective laser melting, Journal of the Mechanical Behavior of Biomedical Materials, 2017, 71, 295–306.
56. Quintana O., Tong W., Effects of oxygen content on tensile and fatigue performance of Ti-6Al-4V manufactured by Selective Laser Melting, The Journal of The Minerals, Metals & Materials Society, 2017, 69, 2693–2697
57. Karolewska K., Ligaj B., Comparison Analysis of Titanium Alloy Ti6Al4V Produced by Metallurgical and 3D Printing Method, Book Series: AIP Conference Proceedings, 2019, 2077, UNSP 020025. DOI: 10.1063/1.5091886
58. Karolewska K., Ligaj B., Wirwicki M., Szala G., Strength analysis of Ti6Al4V titanium alloy produced by the use of additive manufacturing method under static load conditions, Journal of Materials Research and Technology - JMR&T, 2020, 9(2), 1365–1379. https://doi.org/10.1016/j.jmrt.2019.11.063
59. Lu F., et al., Mechanical properties of AlSi10Mg alloy fabricated by laser melting deposition and improvements via heat treatment, International Journal for Light and Electron Optics, 179, 2019, 8–18.
60. Zhang C., Zhu H., Hu Z., Zhang L., Zeng X., A comparative study on single-laser and multi-laser selective laser melting AlSi10Mg: defects, microstructure and mechanical properties, Materials Science & Engineering A, 746, 2019, 416–423.
61. Li Z., et al., Microstructure and Tensile Properties of AlSi10Mg Alloy Manufactured by Multi-Laser Beam Selective Laser Melting (SLM), Metals, 9, 2019, 1337. doi:10.3390/met9121337
62. Maamoun A. H., Elbestawi M. A., Veldhuis S. C., Influence of Shot Peening on AlSi10Mg Parts Fabricated by Additive Manufacturing, J. Manuf. Mater. Process., 2018, 2, 40. doi:10.3390/jmmp2030040
63. Liu X., Zhao C., Zhou X., Shen Z., Liu W., Microstructure of selective laser melted AlSi10Mg alloy, Materials & Design, Volume 2019, 168, 107677.
64. ASTM F3318-18 Standard for Additive Manufacturing. Finished Part Properties. Specification for ALSi10Mg with Power Bed Fusion. Laser Beam.
65. Yakout M., Elbestawi M. A., Veldhuis S. C., Density and mechanical properties in selective laser melting of Invar 36 and stainless steel 316L, Journal of Materials Processing Tech., 2019, 266, 397–420.
66. Zhang Z, Chu B., Wang L., Lu Z., Comprehensive effects of placement orientation and scanning angle on mechanical properties and behavior of 316L stainless steel based on the selective laser melting process, Journal of Alloys and Compounds, 2019, 791, 166–175.
67. Kong D., et. al., Mechanical properties and corrosion behavior of selective laser melted 316L stainless steel after different heat treatment processes, Journal of Materials Science & Technology, 2019, 35, 1499–1507.
68. ASTM F3184 Standard Specification for Additive Manufacturing Stainless Steel Alloy (UNS S31603) with Power Bed Fusion.
69. Bahrami B, Ayatollahi M. R, Torabi A.R, Application of digital image correlation method for determination of mixed mode stress intensity factors in sharp notches, Optics and Lasers in Engineering, 2020, 124, 105830. Available from: https://doi.org/10.1016/j.optlaseng.2019.105830
70. Boniotti L, Beretta S, Patriarca L, Rigoni L, Foletti L, Experimental and numerical investigation on compressive fatigue strength of lattice structures of AlSi7Mg manufactured by SLM, International Journal of Fatigue, 2019, 128, 10518. Available from: https://doi.org/10.1016/j.ijfatigue.2019.06.041
71. Zhang J, Zhang Y, Li W, Karnati S, Liou F, Newkirk J.W, Microstructure and properties of functionally graded materials Ti6Al4V/TiC fabricated by direct laser deposition, Rapid Prototyping Journal, 2018, 24(4), 677–687. Available from: https://doi.org/10.1108/RPJ-12-2016-0215
72. Zhang X, Zhang Y, Wu Y, Ao S, Luo Z, Effects of melting-mixing ratio on the interfacial microstructure and tensile properties of austenitic–ferritic stainless steel joints, Journal of Materials Research and Technology, 2019, 8(3), 2649–2661. Available from: https://doi.org/10.1016/j.jmrt.2018.12.025
73. Marciniak T., Lutowski Z., Bujnowski S., Boronski D., Giesko T., Application of Digital image Correlation in Fatigue Crack Analysis, Fatigue Failure and Fracture Mechanics, Edited by: D. Skibicki, Book Series: Materials Science Forum, 2012, 726, 218. https://doi.org/10.4028/www.scientific.net/MSF.726.218
74. Karolewska K., Ligaj B., Boroński D., Strain analysis of material produced by DMLS technology using Digital Image Correlation, Materials, 2020, 13(15), 3398. https://doi.org/10.3390/ma13153398
75. Segura I. A., et al., Characterization and mechanical properties of cladded stainless steel 316L

with nuclear applications fabricated using electron beam melting, Journal of Nuclear Materials, 2018, 507, 164–176. https://doi.org/10.1016/j.jnucmat.2018.04.026

76. Zhong Y., et al., Additive manufacturing of 316L stainless steel by electron beam melting for nuclear fusion applications, Journal of Nuclear Materials, 2017, 486, 234–245. https://doi.org/10.1016/j.jnucmat.2016.12.042
77. Prekshya N., Debashis N., Guru D. P., Indrani S., Assessment of microstructural evolution and mechanical properties of laser metal deposited 316L stainless steel, Journal of Materials Engineering and Performance, 2021, 30(9), 6996–7006. https://doi.org/10.1007/s11665-021-06101-8
78. Pacheco J. T., et al., Laser directed energy deposition of AISI 316L stainless steel: The effect of build direction on mechanical properties in as-built and heat-treated conditions, Advances in Industrial and Manufacturing Engineering, 2022, 4, 100079. https://doi.org/10.1016/j.aime.2022.100079
79. Lupi G., et al., Fracture toughness of AlSi10Mg alloy produced by direct energy deposition with different crack plane orientations, Materials Today Communications, 2023, 37, 107460. https://doi.org/10.1016/j.mtcomm.2023.107460
80. Austin D., et al., Microstructural investigation and impact testing of additive manufactured TI-6AL-4V, Symposium on Characterization of Minerals, Metals, and Materials in San Diego, Minerals Metals & Materials Series, 2017, 191–199.
81. Biffi C., et al., Effects of the scanning strategy on the microstructure and mechanical properties of a TiAl6V4 alloy produced by electron beam additive manufacturing, The International Journal of Advanced Manufacturing Technology, 2020, 107, 4913–4924.
82. Liu Z., Wang Z., Gao C., Liu R., Xiao Z., Microstructure, anisotropic mechanical properties and very high cycle fatigue behavior of Ti6Al4V produced by selective electron beam melting. Metals and Materials International, 2021, 27, 2550–2561.
83. Pirozzi C., Franchitti S., Borrelli R., Chiariello A., Di Palma L., The effect of post-processing on the mechanical behavior of Ti6Al4V manufactured by electron beam powder bed fusion for general aviation primary structural applications. Aerospace, 2020, 7(6), 75.
84. Kelbassa I., Qualifizieren des Laserstrahl-Auftragschweißens von BLISKs aus Nickel-und Titanbasislegierungen. Ph.D. Thesis, RWTH Aachen University, Aachen, Germany 2006.
85. Qiu C., et al., Fabrication of large Ti–6Al–4V structures by direct laser deposition. J. Alloy. Compd. 2005, 629, 351–361.
86. Keist J. S., Palmer T. A., Role of geometry on properties of additively manufactured Ti-6Al-4V structures fabricated using laser based directed energy deposition. Mater. Des., 2016, 106, 482–494.
87. D'Andrea D., Additive Manufacturing of AISI 316L Stainless Steel: A Review, Metals, 2023, 13(8), 1370. https://doi.org/10.3390/met13081370
88. PN-EN 4267:2004 Aerospace series – Round bars in titanium and titanium alloys
89. PN-EN 10088-2:2014-12 Stainless steels - Part 2: Technical delivery conditions for sheet/plate and strip of corrosion resisting steels for general purposes
90. PN-74/H-04327 Badanie metali na zmęczenie. Próba osiowego rozciągania – ściskania przy stałym cyklu obciążeń zewnętrznych
91. PN-EN ISO 6892-1:2016 Metale – Próba rozciągania – Część 1: Metoda badania w temperaturze pokojowej
92. ISO 6507-1:2018 Metallic materials — Vickers hardness test